Ultramicroscopy 111 (2011) 1029–1036

Contents lists available at ScienceDirect

Ultramicroscopy

journal homepage: www.elsevier.com/locate/ultramic

A fast algorithm for computing and correcting the CTF for tilted, thick specimens in TEM

Lenard M. Voortman [a,*], Sjoerd Stallinga [a], Remco H.M. Schoenmakers [b], Lucas J. van Vliet [a], Bernd Rieger [a,b]

[a] Quantitative Imaging Group, Faculty of Applied Sciences, Delft University of Technology, Lorentzweg 1, 2628 CJ Delft, The Netherlands
[b] FEI Company, Achtseweg Noord 5, 5651 GG Eindhoven, The Netherlands

ARTICLE INFO

Article history:
Received 19 July 2010
Received in revised form
15 December 2010
Accepted 1 March 2011
Available online 8 March 2011

Keywords:
CTF
Tilted geometry
Nonuniform fast Fourier transform
Specimen thickness
TEM
Tomography

ABSTRACT

Today, the resolution in phase-contrast cryo-electron tomography is for a significant part limited by the contrast transfer function (CTF) of the microscope. The CTF is a function of defocus and thus varies spatially as a result of the tilting of the specimen and the finite specimen thickness. Models that include spatial dependencies have not been adopted in daily practice because of their high computational complexity. Here we present an algorithm which reduces the processing time for computing the 'tilted' CTF by more than a factor 100. Our implementation of the full 3D CTF has a processing time on the order of a Radon transform of a full tilt-series. We derive and validate an expression for the damping envelope function describing the loss of resolution due to specimen thickness. Using simulations we quantify the effects of specimen thickness on the accuracy of various forward models. We study the influence of spatially varying CTF correction and subsequent tomographic reconstruction by simulation and present a new approach for space-variant phase-flipping. We show that our CTF correction strategies are successful in increasing the resolution after tomographic reconstruction.

1. Introduction

Cryo-electron tomography (CryoET) is an important tool for studying the three-dimensional (3D) structure of biological specimens in their (close to) native state [1]. In CryoET the 3D scattering potential is reconstructed from many projections at different tilt-angles. The reconstruction of a 3D image from the two-dimensional (2D) projections is typically done using filtered back-projection (FBP) or the simultaneous iterative reconstruction technique (SIRT). The specimens consist mostly of light atoms such as C, N and H, and therefore are very weak electron scatterers. As a result amplitude contrast is not very strong and images are recorded in a phase-contrast mode. This phase contrast is, however, only generated if the specimen is sufficiently defocused to allow interference of the unscattered wave with the scattered wave. The phase-shifts due to elastic scattering are relatively small and are described using the well established weak-phase approximation [2]. Here the image formation is dictated by the contrast transfer function (CTF). The CTF is an oscillating function of the spatial frequency; therefore contrast for certain spatial frequency ranges is inverted. To maximize the transfer of certain spatial frequencies (corresponding to sizes of $\sim 4-10$ nm in the specimen) without contrast inversions, typically several μm underfocus is used in practice. Transmission of higher spatial frequencies is suppressed by the apparent finite source-size of the electron gun. This cut-off point can only be shifted to a higher spatial frequency by using smaller defoci. This comes at the expense of possible contrast inversions in the image. In the presence of these contrast inversions, image interpretation is no longer intuitive. To remove possible contrast inversion, various authors apply a low-pass filter to the projections with its cut-off frequency at the first zero-crossing of the CTF [3,4].

CTF correction is already well established in the field of single-particle analysis [5]. It usually comprises phase-flipping of the spatial frequencies which were imaged with inverted contrast. Sometimes the magnitude of the CTF is also corrected. For each detected particle the defocus is assumed to be constant, which makes CTF correction spatially invariant. When imaging tilted specimens, as in tomography, the assumption that the defocus is constant over the field of view no longer holds. Recently there has been an increased interest to characterize and correct for the effects of this spatially varying CTF [6–11]. As the thickness of the specimen can easily be on the order of 100 nm or more there is also a relevant defocus gradient in the axial direction to be considered [12]. There have also been efforts to correct for these effects [13–16]. The methods described in references [6–16] for forward modeling and for correcting the spatially varying CTF for tilted and/or thick specimens have not

* Corresponding author. Tel.: +31 152783191.
E-mail address: l.m.voortman@tudelft.nl (L.M. Voortman).

0304-3991/$ - see front matter © 2011 Elsevier B.V. All rights reserved.
doi:10.1016/j.ultramic.2011.03.001

been widely adopted for tomographic reconstruction. Partially because of their complexity, but more importantly due to the burden they pose on processing times (for large image sizes up to several weeks). We present a 100-fold reduction of the processing time for the forward modeling of tilted specimens. This makes our spatially varying method for computing CTFs applicable in practice.

The structure of this article is as follows. In Section 2 we present an overview of the different approximations to the CTF: untilted thin, tilted thin and tilted thick. Next, in Section 3 we propose novel algorithms to reduce the computational complexity of modeling a spatially varying CTF. In Section 4 we use simulations to show the limitations and advantages of the different CTF models for forward modeling and finally in Section 5 we apply them to CTF correction.

2. Contrast transfer function for 3D specimens

In order to describe the CTF, we introduce the following terminology. The Fourier transform (FT) of the 3D scattering potential $V(\mathbf{x},z)$ is defined as

$$\hat{V}(\mathbf{q},q_z)=\int V(\mathbf{x},z)e^{-2\pi i(\mathbf{x}\cdot\mathbf{q}+zq_z)}\,d\mathbf{x}\,dz,$$

where $\mathbf{x}=(x,y)$ and $\mathbf{q}=(q_x,q_y)$. Equivalently, we define the 2D FT as $\hat{f}(\mathbf{q})=\int f(\mathbf{x})e^{-2\pi i\mathbf{x}\cdot\mathbf{q}}\,d\mathbf{x}$.

We choose to fix the specimen coordinates $V(\tilde{\mathbf{x}},\tilde{z})$ and rotate the microscope coordinate system $V_\alpha(\mathbf{x},z)$. The rotated coordinate system is defined by two variables: the tilt-angle α and the orientation of the tilt-axis (azimuth) β. Since a rotation of the specimen in real-space corresponds to the same rotation in Fourier space we define[1]

$$\begin{aligned}\hat{V}_\alpha(\mathbf{q},q_z)=\hat{V}(&q_x\cos\beta\cos\alpha+q_y\sin\beta\cos\alpha+q_z\sin\alpha,\\&-q_x\sin\beta+q_y\cos\beta,\\&-q_x\cos\beta\sin\alpha-q_y\sin\beta\sin\alpha+q_z\cos\alpha).\end{aligned}\tag{1}$$

Hence, for $\beta=0$ the tilt-axis is the y-axis, which we will assume in the remainder of this article.

Since scattering in biological specimens is usually very weak, it is common to use the weak-phase approximation [2]. We will use this approximation throughout this article and thus the FT of the recorded intensity is expressed as [17]

$$\hat{I}(\mathbf{q})=2\sin(\chi(q))\hat{V}_\alpha(\mathbf{q},0),\tag{2}$$

with $\chi(q)=(2\pi/\lambda)(\frac{1}{4}C_s\lambda^4q^4+\frac{1}{2}\Delta f\lambda^2q^2)$ the aberration function, C_s is the spherical aberration, Δf is the defocus at $z=0$, λ is the electron wavelength and $q=\|\mathbf{q}\|$. We use the convention that underfocus implies $\Delta f<0$. The projected scattering potential $\hat{V}_\alpha(\mathbf{q},0)$ is equivalent (using the projection slice theorem [18]) to the FT of $\int V_\alpha(\mathbf{x},z)\,dz$.

We ignore amplitude contrast in Eq. (2) to keep the following derivations short and to improve the readability. In practice, amplitude contrast can be incorporated simply as an additional phase-shift [2].

Note that Eq. (2) is an approximation to the full contrast transfer function as the defocus is assumed to be constant for the whole specimen. We will refer to Eq. (2) as CTF_0.

2.1. Tilted, thin specimens

To allow for tilted geometries Philippsen et al. [6] derived an extension to the CTF_0. We will refer to this function (which they called the tilted contrast-imaging function) as the tilted CTF (TCTF). The FT of the recorded image intensity for tilted, thin specimens is

$$\hat{I}(\mathbf{q})=ie^{-i\chi(q)}\hat{V}_\alpha(\mathbf{q}-\tfrac{1}{2}\lambda q^2\boldsymbol{\beta}\tan\alpha,0)-ie^{i\chi(q)}\hat{V}_\alpha(\mathbf{q}+\tfrac{1}{2}\lambda q^2\boldsymbol{\beta}\tan\alpha,0),\tag{3}$$

where $\boldsymbol{\beta}$ is a unit-vector perpendicular to the tilt-axis with $\boldsymbol{\beta}=(\cos\beta,\sin\beta)$. For small tilt-angles, i.e. $\alpha\to0$, Eq. (3) gradually reduces to Eq. (2).

2.2. Thick specimens

The validity of Eq. (2) is not only limited to untilted specimens, but is also limited to thin specimens. In the weak-phase regime all scattering events can be treated as weak and independent. Therefore all points in the specimen contribute linearly to the recorded intensity. Incorporating the effects of the thickness of the specimen is simply a matter of integrating along the z-direction of the scattering potential times the appropriate CTF

$$\hat{I}(\mathbf{q})=\int 2\sin(\chi(q)-\pi\lambda zq^2)\mathcal{F}_{\mathbf{x}}[V_\alpha(\mathbf{x},z)]\,dz.\tag{4}$$

Wan et al. [12] showed that the evaluation of Eq. (4) can be simplified by taking the FT in the z-direction

$$\mathcal{F}_z[2\sin(\chi(q)-\pi\lambda zq^2)]=ie^{-i\chi(q)}\delta(q_z-\tfrac{1}{2}\lambda q^2)-ie^{i\chi(q)}\delta(q_z+\tfrac{1}{2}\lambda q^2).\tag{5}$$

Using this equation, the multiplication in Eq. (4) of the scattering potential with the CTF can be written as a convolution in q_z. The integration over z is equal to evaluating for $q_z=0$. Combining these steps leads to [12]

$$\hat{I}(\mathbf{q})=ie^{-i\chi(q)}\hat{V}_\alpha(\mathbf{q},-\tfrac{1}{2}\lambda q^2)-ie^{i\chi(q)}\hat{V}_\alpha(\mathbf{q},\tfrac{1}{2}\lambda q^2),\tag{6}$$

which we will refer to as the three-dimensional CTF (3DCTF). We show in the following section that Eq. (6) reduces to Eq. (3) for infinitely thin specimens. Here we also derive the approximation error of Eq. (3) with respect to Eq. (6).

2.3. Thickness induced damping envelope

One very common assumption in Cryo-ET is that the 3D scattering potential can be approximated by a 2D projected scattering potential. The TCTF (Eq. (3)) is an approximation to the 3DCTF (Eq. (6)) for thin specimens. We will quantify the correctness of this approximation as a function of the specimen thickness. In order to show the relation between these two equations, we first ideally describe a specimen with limited thickness as

$$V(\tilde{\mathbf{x}},\tilde{z})=V_\infty(\tilde{\mathbf{x}},\tilde{z})\frac{1}{t}\text{rect}\left(\frac{\tilde{z}}{t}\right),\tag{7}$$

where $V_\infty(\tilde{\mathbf{x}},\tilde{z})$ is a theoretical specimen with infinite thickness, t is the thickness of the real specimen $V(\tilde{\mathbf{x}},\tilde{z})$ and $(1/t)\text{rect}(\tilde{z}/t)$ is a normalized block function of unity area. A multiplication with the block function in Eq. (7) is equivalent to

$$\hat{V}(\tilde{\mathbf{q}},\tilde{q}_z)=\hat{V}_\infty(\tilde{\mathbf{q}},\tilde{q}_z)\star\text{sinc}(t\tilde{q}_z),\tag{8}$$

where $\star$ is the convolution operator in $\tilde{q}_z$ and $\text{sinc}(t\tilde{q}_z)$ is the normalized sinc function. For infinitely thin specimens, $\hat{V}(\tilde{\mathbf{q}},\tilde{q}_z)$ is independent of $\tilde{q}_z$.

Revisiting the TCTF (Eq. (3)) and the 3DCTF (Eq. (6)) we see that the scattering potential $\hat{V}_\alpha$ is sampled, in the microscope coordinates, at $(\mathbf{q}\mp\frac{1}{2}\lambda q^2\boldsymbol{\beta}\tan\alpha,0)$ and $(\mathbf{q},\mp\frac{1}{2}\lambda q^2)$, respectively. For a graphical representation see Fig. 1. From this figure (or from Eq. (1)) we see that the lateral (in the specimen coordinates) spatial frequency axes $(\tilde{q}_x,\tilde{q}_y)$ coincide. Along the axial spatial frequency, however, there is a discrepancy of

$$\Delta\tilde{q}_z=\frac{1}{2}\lambda q^2(\sin\alpha\tan\alpha+\cos\alpha)=\frac{1}{2}\lambda q^2\frac{1}{\cos\alpha}.$$

[1] We implicitly define $\hat{V}(\tilde{q}_x,\tilde{q}_y,\tilde{q}_z)=\hat{V}(\tilde{\mathbf{q}},\tilde{q}_z)$.

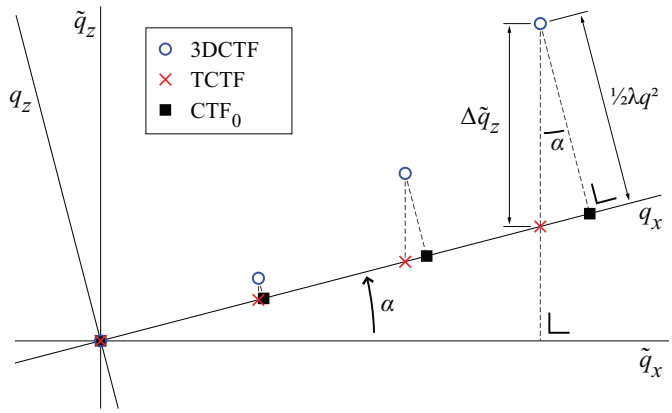

Fig. 1. A comparison of the CTF_0, TCTF and 3DCTF based on the points sampled in Fourier space ($\beta=0$). The rotated axes (q_x,q_z) correspond to the coordinate system of the microscope, perpendicular to the tilt-axis. As a result, $\hat{V}_\alpha(\mathbf{q},0)$ is the central section which represents the projection data under a certain tilt-angle. The fixed axes $(\tilde{q}_x,\tilde{q}_z)$ correspond to the Fourier space of the specimen: $\hat{V}(\tilde{\mathbf{q}},\tilde{q}_z)$. The relation between $\hat{V}_\alpha$ and $\hat{V}$ is described by Eq. (1). For clarity, only $\hat{V}_\alpha(\mathbf{q},0)$ (■), $\hat{V}_\alpha(\mathbf{q}+\frac{1}{2}\lambda q^2\boldsymbol{\beta}\tan\alpha,0)$ (×) and $\hat{V}_\alpha(\mathbf{q},+\frac{1}{2}\lambda q^2)$ (○) for $\mathbf{q}\geq 0$ and $q_y=0$ are plotted. Here $\alpha<0$.

In combination with Eq. (8) we conclude that the fraction of the transferred signal is given by

$$E_{t,\alpha}(\mathbf{q})=\operatorname{sinc}\left(\frac{1}{2}\lambda q^2\frac{t}{\cos\alpha}\right), \tag{9}$$

if instead of sampling $\hat{V}(\tilde{\mathbf{q}},\tilde{q}_z)$ we sample $\hat{V}(\tilde{\mathbf{q}},\tilde{q}_z+\Delta\tilde{q}_z)$. This function can be used to estimate the overall loss of resolution when a specimen with thickness t is approximated by an infinitely thin specimen. Neglecting the thickness produces the effect of a damping envelope, similar to the spatial and temporal damping envelopes [17, Section 6.4.2].

From Eq. (9) we also see that in the limit of an infinitely thin specimen ($t\to 0$), Eq. (3) can be used instead of Eq. (6) without loss of transfer.

3. Algorithmic improvements

The effects of tilting and/or specimen thickness on the CTF have not been widely adopted in reconstruction or forward modeling due to the large burden they pose on processing times. Even though Eq. (2) of the CTF_0 and Eq. (3) of the TCTF look very similar, their discrete counterparts highlight some challenging differences. The function $\hat{V}_\alpha(\mathbf{q},0)$ in Eq. (2) can be discretized by sampling on a regular grid. This results in a discrete Fourier transform (DFT) which can be computed by a standard fast Fourier transform (FFT). In contrast, the samples of $\hat{V}_\alpha$ in Eq. (3) do not form a regular grid ($\mathbf{q}\mp\frac{1}{2}\lambda q^2\boldsymbol{\beta}\tan\alpha$). These sample points do not coincide (in general) with the discretized spatial frequencies of the DFT. As a result the FFT cannot be used to compute $\hat{V}_\alpha$.

Let us first consider the general case of spatially varying filtering

$$I(\mathbf{x})=\int V(\mathbf{s})h(\mathbf{x}-\mathbf{s},\mathbf{s})\,d\mathbf{s}, \tag{10}$$

where $h(\mathbf{x},\mathbf{s})$ is a spatially varying point-spread function corresponding to the input (object) V at location $\mathbf{s}$. We can relate the point-spread function to a transfer function $T(\mathbf{q},\mathbf{s})$ in the Fourier domain by

$$h(\mathbf{x},\mathbf{s})=\int T(\mathbf{q},\mathbf{s})e^{2\pi i\mathbf{q}\cdot\mathbf{x}}\,d\mathbf{q}. \tag{11}$$

For example, the transfer function corresponding to the CTF_0 is simply $T_{CTF}(\mathbf{q},\mathbf{x})=2\sin(\chi(q))$. The extension to a spatially varying transfer function T_{TCTF} is given by

$$T_{TCTF}(\mathbf{q},\mathbf{x})=2\sin(\chi(q)-\pi\lambda q^2\mathbf{x}\cdot\boldsymbol{\beta}\tan\alpha). \tag{12}$$

To derive a general expression for a spatially varying transfer function, let us insert Eq. (11) into Eq. (10) and change to the Fourier domain $\hat{I}(\mathbf{p})$ ($\mathbf{q}$ is already in use by $T(\mathbf{q},\mathbf{s})$). Now we can first integrate over $\mathbf{x}$ which results in a $\delta(\mathbf{q}-\mathbf{p})$ term. Then, integrate over $\mathbf{q}$ and replace the remaining $\mathbf{p}$ by $\mathbf{q}$. This leads us to the following result:

$$\hat{I}(\mathbf{q})=\int V(\mathbf{x})T(\mathbf{q},\mathbf{x})e^{-2\pi i\mathbf{q}\cdot\mathbf{x}}\,d\mathbf{x}, \tag{13}$$

where $V(\mathbf{x})$ is the input scattering potential, $T(\mathbf{q},\mathbf{x})$ is a spatially varying transfer function and $\hat{I}(\mathbf{q})$ is the output with $\mathbf{x},\mathbf{q}\in\mathbb{R}^2$.

Evaluation of $\hat{I}(\mathbf{q})$ in the form of Eq. (13) can only be implemented for discretized data as a matrix multiplication. In contrast, when $T(\mathbf{q},\mathbf{x})$ does not depend on the location $\mathbf{x}$, Eq. (13) simplifies to $\hat{I}(\mathbf{q})=\hat{V}(\mathbf{q})T(\mathbf{q},0)$. Such spatially invariant equations can clearly be computed much faster. They can be implemented using the FFT algorithm which has a computational complexity of $\mathcal{O}(N\log N)$ [19] compared to $\mathcal{O}(N^2)$ for a regular DFT or matrix multiplication needed to compute Eq. (13).

3.1. Nonuniform fast Fourier transform

One way of implementing the TCTF (Eq. (3)) is to revert to a set of linear equations similar to Eq. (13) with Eq. (12) as a transfer function (as done by Philippsen et al. [6]). We developed an algorithm which results in a substantially faster implementation.

The TCTF of Eq. (3) is presented as two separate terms each sampling the FT of the scattering potential at slightly different points. Computing the Fourier transform of a nonuniform grid of points is, however, not straightforward. We propose to compute this Fourier transform by using the nonuniform fast Fourier transform (NUFFT) (also called gridding) [20,21]. Here we have used a specific implementation which uses a Gaussian kernel [22].

The fact that the CTF for tilted (TCTF, Eq. (3)) and/or thick (3DCTF, Eq. (6)) specimens can be computed by nonuniform sampling in the Fourier domain is a result of the particular (oscillating) cos-like dependence of the CTF as a function of defocus and not a general property of spatially varying transfer functions. For example, this does not work for the finite source-size envelope because the FT in the axial direction does not result in a (finite) set of δ-functions.

3.2. Taylor expansion of transfer functions

In order to speed up the calculation of those space-variant transfer functions for which the FT does not result in a finite set of δ-functions, we propose a Taylor series approximation. The Taylor series of $T(\mathbf{q},\mathbf{x})$ in $\mathbf{x}$ combined with Eq. (13) yields

$$\hat{I}(\mathbf{q})=\sum_{n=0}^{n_{max}}\frac{T^{(n)}(\mathbf{q},0)}{n!}\mathcal{F}_{\mathbf{x}}[\mathbf{x}^n V(\mathbf{x})]+\mathcal{O}(n_{max}+1), \tag{14}$$

with $T^{(n)}(\mathbf{q},0)=\partial^n T(\mathbf{q},\mathbf{x})/\partial\mathbf{x}^n|_{\mathbf{x}=0}$ and n_{max} the order at which the Taylor series is truncated. The derivatives of $T(\mathbf{q},\mathbf{x})$ can be derived analytically which make their implementation straightforward. At the expense of a summation over $n_{max}+1$ terms, Eq. (14) can now be implemented using the FFT. Fortunately, when the spatial dependence is weak, the Taylor series can be truncated after a relatively small number of terms.

In Appendix A we present an implementation for the finite source-size envelope in the form of Eq. (14) as well as an illustrative example.

The processing time for Eq. (14) depends linearly on the number of terms. The approximation error of the expansion can be estimated from Taylor series theory. To achieve a certain

Table 1
Average run-times for two different methods to calculate the TCTF (Eq. (3)) are shown: (first row) the full linear model of Eq. (13) using Eq. (12) and (second row) the NUFFT method described in the text. Rows 3 and 4 show the average run-times of, respectively, the build-in Matlab function and the NUFFT for calculating the Radon transform. The last row shows the average run-time of a combination of the Radon transform and the 3DCTF (Eq. (6)) using the NUFFT. Notice that some values are in minutes (m) and some in hours (h).

Image size (pixel) Method	1024^2 Runtime	2048^2	4096^2
TCTF, Eq. (13)	83.1m	12.3h	95.9h
TCTF, 1D NUFFT	2.9m	11.3m	44.4m
Radon, Matlab	14.2m	1.9h	14.9h
Radon, 2D NUFFT	14.0m	1.8h	13.3h
3DCTF, 2D NUFFT	18.3m	2.1h	14.5h

Values represent averages over 100 2D image slices, each projected for 141 tilt-angles. Standard deviations were all below 5%.

accuracy requires a lower order of the expansion for low tilt-angles than for higher tilt-angles. Therefore we change the order n_{max} adaptively depending on the tilt-angle and some specific microscope parameters.

3.3. Speed improvement

In order to evaluate the improvements in processing times for each of the proposed methods, we implemented them to simulate a full tilt-series for an artificial specimen. The processing times of the different methods only depend on the image size N^2. All methods were implemented in Matlab (The MathWorks, USA) and the results are shown in Table 1. Without loss of generality the 3D (x,y,z) specimen was reduced to a set of 2D (x,z) slices perpendicular to the tilt-axis. For each 2D slice, a tilt-series of 141 1D projections with a maximum tilt-angle of $\pm 70^\circ$ was simulated. Processing times were evaluated on a PC equipped with an Intel E8400 dual core 3 GHz processor and 8 GB RAM. The processing times of the 1D projections were scaled to resemble the computation of a full tilt-series where the 2D projections have a square image size.

To calculate the TCTF (Eq. (3)) efficiently one takes the 1D NUFFT of each projection in the tilt-series at the appropriate spatial frequencies. In Table 1 we show that this approach is more than two orders of magnitude faster for an image size of 4096^2 than by computing Eq. (13) through a full matrix multiplication (along a single image dimension). We also noticed that simulating the TCTF using the 1D NUFFT is only four times slower than simulating CTF_0. This means that the TCTF is now within reach for iterative reconstruction algorithms.

Next to the speed advantage, implementing the TCTF using the 1D NUFFT is also intuitive and does not depend on any additional parameters such as strip width or tile size as required by other approaches [7,9–11] where the image is split into (overlapping) strips or tiles of approximately equal defocus for processing.

To calculate the 3DCTF (Eq. (6)) the 2D NUFFT of the scattering potential must be calculated at the appropriate spatial frequencies.[2] The 2D NUFFT can also be used to compute forward projections [23]. Table 1 shows that this approach results in processing times of the same order as the (real-space) Radon transform implemented in Matlab. When calculating the 3DCTF one implicitly projects the (x,z) slice of the scattering potential to a 1D signal. We further notice that simulating the 3DCTF indeed results in processing times of the same order as calculating the forward projection using the 2D NUFFT.

[2] Since we calculate each (x,z) slice of the 3D scattering potential independently, a 2D NUFFT is sufficient.

4. Simulating the effects of the complete CTF

In the previous sections we presented three different forward models and explored their relation:

1. untilted, thin specimens: CTF_0, Eq. (2);
2. tilted, thin specimens: TCTF, Eq. (3);
3. tilted, thick specimens: 3DCTF, Eq. (6).

In this section we will investigate the frequency transfer characteristics of these models using simulations.

4.1. White noise test specimen

To compare the different forward models a specimen model is required. To avoid a bias toward a specific spatial frequency range, a synthetic specimen with a flat spectrum is desirable. Therefore, we choose white noise as an input specimen. To overcome the inherent stochastic nature of such a specimen, the results of 150 realizations are averaged.

We also reduce the 3D (x,y,z) problem to 2D (x,z) slices perpendicular to the tilt-axis. Without loss of generality this reduces the processing time while maintaining the full complexity of the problem. We simulate specimens with a thickness of 50, 100 and 200 nm and a field of view (FOV) of 1 μm. We avoid local-tomography effects [24,25]. We also do not consider possible loss of resolution and additional noise at detection by plate or CCD camera, given by the modulation transfer function [26].

The CTF_0 and TCTF forward models both act on projected data (which is 1D in the following simulations). The 3DCTF, however, is a function of the 2D (x,z) slice. In order to avoid aliasing effects sufficient zero-padding in the z-direction is required. The specimen is padded with zeros to make the (x,z) slice square. We verified that the amount of zero-padding is sufficient by comparing projections generated using the regular Radon transform with those generated by direct sampling using the NUFFT.

4.2. Forward modeling

If a forward model is used in an iterative reconstruction algorithm, its computational complexity is of great importance. A trade-off has to be made between the accuracy (or correctness) of a forward model and its computational complexity.

We simulated projections of the white noise test specimen with the three different forward models mentioned above: CTF_0, TCTF and 3DCTF. To test the accuracy of the two approximations (CTF_0 and TCTF), we compare projections generated by these models with projections generated with the 3DCTF forward model. The microscope parameters were set to: $\Delta f = -1$ μm, $\lambda = 2.5$ pm (HT = 200 kV), $C_s = 2$ mm and the convergence angle $\alpha_i = 0.2$ mrad (see Appendix A). The 1D projections consisted of 4096 pixels with a pixel size of 0.24 nm.

In order to verify the quality of the different forward models, i.e. the resolution, a comparison of the projections is required. There are numerous ways to measure the resolution in a reconstructed volume. In the field of single-particle analysis, Fourier shell correlation (FSC) is used extensively to check the consistency of a reconstruction [27,28]. There the initial dataset is usually split into two and each half is used to reconstruct the particle after which the two reconstructions are correlated with each other. For our purpose, we define the normalized Fourier correlation (NFC) of two functions f and g as the 1D equivalent of

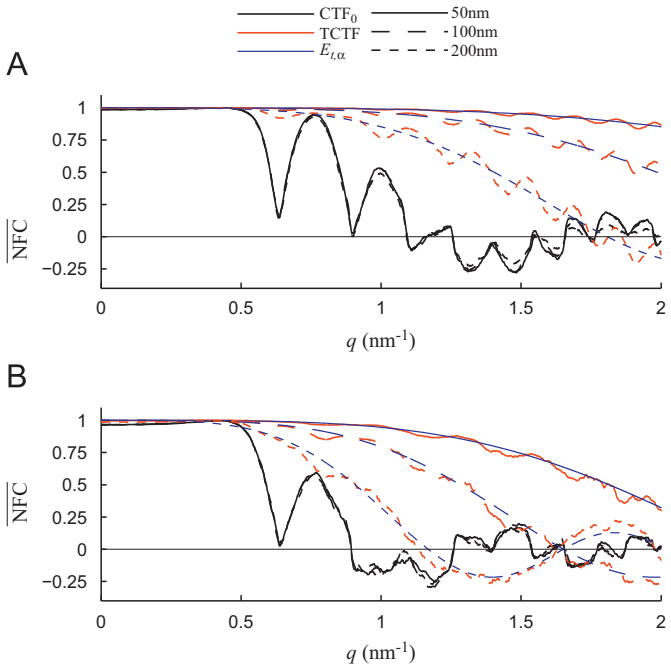

Fig. 2. Average NFC over 150 realizations between the 3DCTF and the two approximations: CTF_0 in black, TCTF in red. The simulations were carried out for specimens with a thickness of 50, 100 and 200 nm. Overlaid in blue is Eq. (9), the analytic prediction of the resolution loss (damping envelope) as a result of neglecting the specimen thickness. (A) Specimen tilted at 35°; (B) specimen tilted at 70°. (For interpretation of the references to color in this figure legend, the reader is referred to the web version of this article.)

Fourier ring correlation (FRC) and Fourier shell correlation (FSC)

$$\mathrm{NFC}_{f,g}(\mathbf{q}) = \frac{\sum_{\mathbf{q}' \in \mathbf{q}_i} \hat{f}(\mathbf{q}')\hat{g}^*(\mathbf{q}')}{\sqrt{\sum_{\mathbf{q}' \in \mathbf{q}_i} \|\hat{f}(\mathbf{q}')\|^2 \sum_{\mathbf{q}' \in \mathbf{q}_i} \|\hat{g}(\mathbf{q}')\|^2}}, \tag{15}$$

where $\mathbf{q}_i$ is a small range of spatial frequencies around $\mathbf{q}$ and $-\mathbf{q}$.

In Fig. 2 we show the result of the NFC between the two approximate models (CTF_0 and TCTF) and the 3DCTF. From this figure we conclude that the loss of transfer when using the projection assumption can be estimated using Eq. (9). From Fig. 2 we also conclude that for specimens tilted up to $\pm 70°$, with a thickness of 100 nm or less the TCTF is a very good approximation to the 3DCTF for spatial frequencies up to (at least) 1.3 nm^{-1}. The expected loss of resolution (Eq. (9)) when using TCTF instead of 3DCTF agrees very well with the simulations. This implies that the accuracy of the TCTF can be approximated accurately with the help of Eq. (9). Eq. (9) can also be useful to find the tolerable thickness or alternatively to estimate the achievable resolution using the TCTF.

Furthermore, we see in Fig. 2 that for CTF_0, the results only slightly vary when changing the thickness. However, it is also clear that the CTF_0 is only a valid approximations up to approximately 1 nm^{-1} for specimens tilted at $\pm 35°$ and only up to 0.7 nm^{-1} at $\pm 70°$. The clearly visible zero-crossings of the CTF for the CTF_0 result (indicated by the steep dips of the $\overline{\mathrm{NFC}}$) are in some way also present in the TCTF model. But in the TCTF model the defocus varies spatially, and as a result the zero-crossings do as well. Hence, parts without contribution (the zero-crossings) are averaged with parts of non-zero contribution.

5. CTF correction

Next to forward modeling of the CTF, one ultimately wants to correct for these effects in order to reconstruct an unambiguous (without phase-reversals) estimate of the specimen under investigation. We are interested how much the resolution in a reconstructed tomogram can be improved as a result of proper correction for the CTF with spatially varying defocus.

To this end we simulated a tilt-series of 141 projections using the 3DCTF with an underfocus of 1 μm (tilt-angles were uniformly distributed between $\pm 70°$). White noise was again used as a specimen model. The thickness of the specimen was 100 nm. The 1D projections consisted of 4096 pixels with a pixel size of 0.24 nm. For more details we refer to Section 4 in which the same settings are used.

Poisson noise was added to the projections to simulate realistic low-dose noise conditions. We used a total dose of $150e^-/\mathrm{Å}^2$ for the entire tilt-series, assuming that the signal of the 1D projections represents a line of square pixels (this corresponds to ~ 6.3 counts per pixel per tilt-angle). The modulation depth of the phase-contrast signal was set to 10%.

5.1. Tomographic reconstruction

There exists a variety of algorithms to reconstruct a specimen from its projections. Here we used filtered back-projection (FBP) because compared to other algorithms this method depends on the smallest number of parameters. This allows us to do a comparison of reconstructions which depends primarily on the different CTF correction methods and not on how well we succeeded in the fine-tuning of the reconstruction algorithm.

In Fig. 3 we show the results for the three different CTF correction methods (discussed below) after tomographic reconstruction. To analyze the difference in the lateral direction ($\mathbf{x}$) we calculate the NFC in the z-direction of the reconstruction.

In a simulation the specimen is known. We therefore choose to correlate the different reconstructions to the original specimen. This results in relatively low correlation values. We also correlated the reconstruction to a reconstruction of the undistorted projections. Both suffer from the same 'missing wedge' artifact and therefore correlate much better. Nevertheless, we settled for correlating to the original specimen because this leads to the most objective measure of resolution. The choice of tomographic reconstruction method also affects the absolute correlation values. It is well accepted that iterative reconstruction methods, such as SIRT, perform much better under noisy conditions. Nevertheless, the results in Fig. 3 show a clear difference between the different CTF correction methods.

5.2. Phase-flipping

The two most common methods for CTF correction in Cryo-ET are phase-flipping (which corrects the parts of the frequency domain data which have negative contrast) and amplitude correction [7,10,11]. We also implemented and tested amplitude correction using a Wiener filter approach, but we opted for phase-flipping because this gives the best results under the chosen noise conditions.

To apply phase-flipping to tilted specimens we developed the following approach. The TCTF is written in the form of Eq. (13), leading to a transfer function T_{TCTF} given by Eq. (12). Subsequently, our CTF correction algorithm is described by

$$V'(\mathbf{x}) = \int \hat{I}(\mathbf{q})\mathrm{sgn}(T_{TCTF}(\mathbf{q},\mathbf{x}))e^{-2\pi i \mathbf{q}\cdot\mathbf{x}}\, d\mathbf{q}, \tag{16}$$

where $V'(\mathbf{x})$ is an estimate of $V(\mathbf{x})$ and $\mathrm{sgn}(x)$ is the sign function.

When we compare the result of CTF_0 phase-flipping in Fig. 3A with the result of TCTF phase-flipping of Eq. (16) in Fig. 3B we see a dramatic increase in resolution at the edges of the specimen ($x = \pm 500$ nm). Around the tilt-axis ($x = 0$ nm) the difference

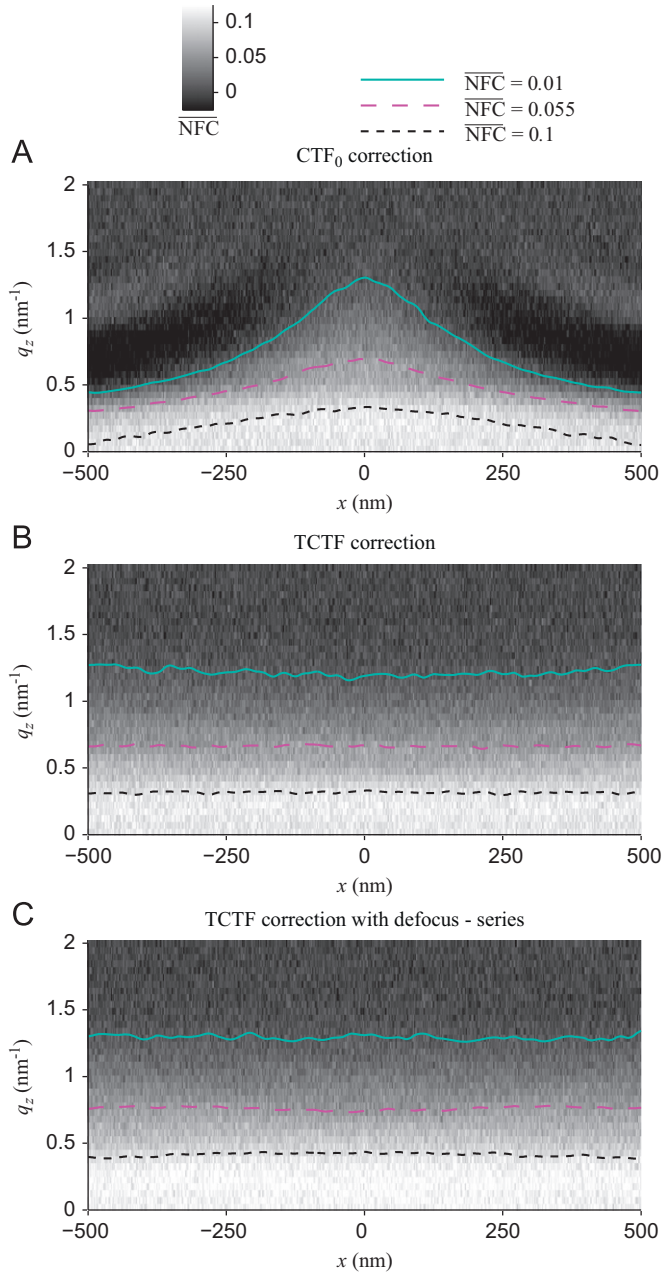

Fig. 3. Average NFC between an (x,z) slice of the CTF corrected reconstruction and the original (known) specimen over 150 realizations. Simulated projections were CTF corrected without accounting for spatially varying defocus (A), with correction of spatially varying defocus (B), and finally by combining different defocus values and spatially varying defocus correction (C). All CTF correction methods use phase-flipping. Isolines are plotted for easier comparison. The average difference of the NFC between (B) and (C) is 16% of the average value of (B).

between the two methods disappears because tilting the specimen does not induce a significant difference in defocus.

5.3. Defocus-series

The zero-crossings of the CTF make it impossible to obtain a good estimate of $V(\mathbf{x})$ (from a single projection) because at these points in the Fourier domain all information about the specimen is lost. A solution to this problem is to acquire a defocus-series after which the different projections can be combined to estimate $V(\mathbf{x})$ [29].

We propose to (also) apply this approach to tomography by acquiring a defocus-series at each tilt-angle of a tilt-series while not increasing the total dose. The dose available for a certain tilt-angle is distributed over the defocus-series. Note that this does not influence the signal-to-noise (SNR) ratio of the estimate $V'(\mathbf{x})$ [30]. It will, however, result in lower SNR per recording which might hamper the alignment procedure in practice. Assuming that a perfect alignment exists, we investigated whether a defocus-series will result in an increased resolution.

We simulated a defocus-series of three different average defocus values: -0.5, -1 and -1.5 μm, at each tilt-angle. This choice was made to properly correct for the first zero-crossing ($q = 0.63$ nm^{-1}) at a defocus of -1 μm. CTF correction for defocus-series is usually done with a modified Wiener filter [29], our experience with this approach is that it is too sensitive to noise. We chose an alternative method which resembles phase-flipping for a single projection. This requires no regularization and gives better results under our noise conditions. The CTF correction for each defocus-series at a certain tilt-angle is given by

$$\hat{V}'(\mathbf{q}) = \frac{\sum_i \hat{V}_i'(\mathbf{q})}{\sqrt{\sum_i \int T_i(\mathbf{q},\mathbf{x})^2 \, d\mathbf{x}}}, \tag{17}$$

where the summation runs over the different defocus values and $\hat{V}_i'(\mathbf{q})$ is the FT of

$$V_i'(\mathbf{x}) = \int \hat{I}_i(\mathbf{q}) T_i(\mathbf{q},\mathbf{x}) e^{-2\pi i \mathbf{q}\cdot\mathbf{x}} \, d\mathbf{q}.$$

This reduces to regular phase-flipping for a single untilted projection.

In Fig. 3C we notice that distributing the dose at each tilt-angle over three projections at different defocus values has the potential to increase the achievable resolution compared to TCTF phase-flipping of a single projection as shown in Fig. 3B. The advantage of the defocus-series based TCTF correction of Eq. (17) is that it does not require regularization and that it will not amplify noise because the magnitude per spatial frequency stays fixed.

5.4. Influence of defocus accuracy

So far we have assumed that the exact defocus is known as an input to the CTF correction step. In reality, the defocus needs to be estimated. It is therefore important to investigate the sensitivity of the discussed methods to an error in the defocus estimation. To this end we simulated a tilt-series with an underfocus of 1 μm and subsequently used a slightly different systematic defocus value for CTF correction of the tilt-series. The results of these simulations are shown in Fig. 4A.

Judging from Fig. 4A, a systematic error in defocus estimation on the order of 50 nm is acceptable when using TCTF correction (possibly with defocus-series). The thickness of the simulated specimen was 100 nm which also introduces an ambiguity of the defocus for the TCTF method. CTF_0 correction shows much less dependence on an error in the defocus estimation. This result is expected since for tilted specimens CTF_0 correction based on an erroneous defocus value is still valid for some parts of the projection.

Next to a systematic error in defocus estimation, the defocus for each projection in a tilt-series is not constant [11,10]. We have also investigated the sensitivity of CTF correction to these fluctuations by imposing a normal distributed stochastic defocus error to each projection of the tilt-series. The result is shown in Fig. 4B. When compared to a systematic defocus error (shown in Fig. 4A) the effects are almost the same. Only for larger stochastic errors the influence is slightly smaller.

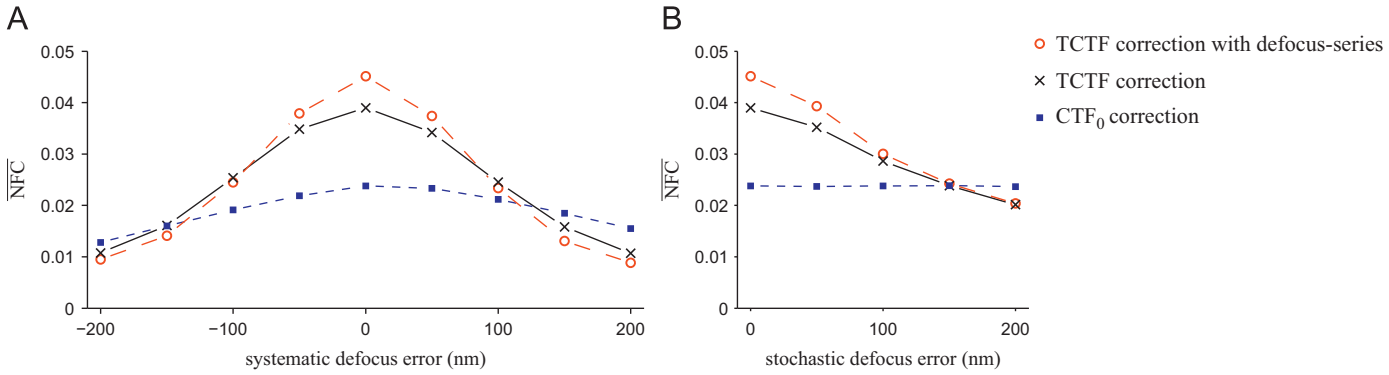

Fig. 4. Averaged NFC values as seen in Fig. 3 using the discussed CTF correction methods but with an erroneous defocus for the CTF correction step. Systematic defocus error for all projections (A). Positive values are closer to focus. Normal distributed defocus error for each projection (B).

6. Conclusions

We derived an analytical expression for the loss of resolution by using the projection assumption, i.e. ignoring the actual thickness of the specimen Eq. (9). This estimated loss of resolution was verified by the simulation of projections at different tilt-angles and specimen thicknesses. Eq. (9) can now be used as a rule-of-thumb for estimating whether the projection assumption is sufficient to image at a certain resolution, or alternatively to estimate up to which resolution the TCTF is a good approximation to the 3DCTF. For actual acquisitions of a specimen with a certain thickness the transfer beyond a certain spatial frequency is severely damped. With the help of Eq. (9) the signal-to-noise ratio of each projection can now be increased by insertion of the correct objective aperture that blocks the scattered waves above this frequency.

We successfully reduced the processing time required for computing the TCTF by more than a factor 100. The processing time of the 3DCTF is reduced to the time it takes to compute one Radon transform. We anticipate that this reduction of processing time will commence the development of new iterative reconstruction algorithms which incorporate these models to improve the resolution of reconstructed tomograms.

We used simulations to quantify the effects of the specimen thickness on the accuracy of the TCTF and CTF_0. This yields a first indication of the applicability of the TCTF for specimens of finite thickness. In contrast to [6], who used a direct inversion of projections simulated by the TCTF, we applied TCTF correction to projections simulated by the 3DCTF. This approach is much closer to reality and therefore provides a better view on the applicability of the TCTF for CTF correction.

The approach taken by [6,8] for CTF correction is based on the direct inversion of the TCTF operator, without regularization and with truncated singular value decomposition, respectively. We proposed a new method for TCTF correction which resembles phase-flipping of the CTF_0. It does not require regularization and cannot amplify noise. Furthermore, we also described a phase-flipping-like TCTF correction method for defocus-series. Finally we showed that these CTF correction strategies are successful in increasing the resolution after tomographic reconstruction.

Acknowledgment

L.M. Voortman was financially supported by the FOM Industrial Partnership program No. 07.0599.

Appendix A. Taylor expansion of transfer functions

As an illustrative example we have worked out the first three terms of Eq. (14) using the T_{TCTF} (Eq. (12)) as a transfer function:

$$\begin{aligned}\hat{I}(\mathbf{q}) = {} & 2\sin(\chi(q))\mathcal{F}_{\mathbf{x}}[V(\mathbf{x})] \\ & -2\cos(\chi(q))(\pi\lambda q^2\tan\alpha)\mathcal{F}_{\mathbf{x}}[(\mathbf{x}\cdot\boldsymbol{\beta})V(\mathbf{x})] \\ & -\sin(\chi(q))(\pi\lambda q^2\tan\alpha)^2\mathcal{F}_{\mathbf{x}}[(\mathbf{x}\cdot\boldsymbol{\beta})^2V(\mathbf{x})]+\cdots. \end{aligned} \tag{A.1}$$

Notice that Eq. (A.1) is merely meant as an example to illustrate how Eq. (14) should be interpreted. The TCTF can be implemented using the much faster NUFFT algorithm described earlier.

In order to accurately describe the imaging model for thick tilted specimens, the finite source-size envelope needs to be reconsidered. As derived by [17, Section 6.4.2] the envelope function belonging to the effects of the finite source-size is

$$\begin{aligned} K_s(q) &= \exp\left(-\frac{(\nabla\chi(q))^2H^2}{4\ln 2}\right) \\ &= \exp\left(-\frac{(\pi C_s\lambda^2q^3-\pi\Delta f q)^2\alpha_i^2}{\ln 2}\right), \end{aligned}$$

where $\nabla\chi(q)$ is the gradient of the aberration function, $H=\alpha_i/\lambda$, and α_i is the convergence angle. Since this envelope depends on Δf, it must be reconsidered for thick and/or tilted specimens. We define the spatially varying finite source-size envelope as

$$K_{s,z}(\mathbf{q},z) = \exp\left(-\frac{(\nabla\chi(q)-\pi\lambda z q)^2H^2}{4\ln 2}\right),$$

where z is the deviation from the average defocus. Applying Eq. (14) leads to

$$\hat{I}_{K_s}(\mathbf{q}) = \sum_{n=0}^{n_{max}} \frac{K_{s,z}^{(n)}(\mathbf{q},0)}{n!}\mathcal{F}_{\mathbf{x}}[(\mathbf{x}\cdot\boldsymbol{\beta}\tan\alpha)^nI(\mathbf{x})], \tag{A.2}$$

where

$$\begin{aligned}\frac{K_{s,z}^{(n)}(\mathbf{q},0)}{n!} &= \left.\frac{\partial^nK_{s,z}(\mathbf{q},z)}{\partial z^n}\right|_{z=0}\frac{1}{n!} \\ &= K_s(q)\sum_{k=0}^{n}A_{n,k}(\nabla\chi(q))^k\left(\frac{H}{2\sqrt{\ln 2}}\right)^{k+n},\end{aligned}$$

and with

$$A_{n,k} = \begin{cases} (-1)^{((n-k)/2)}\dfrac{2^k}{\left(\frac{n-k}{2}\right)!k!} & \text{if } n-k \text{ is even and } k<n, \\ 0 & \text{otherwise.}\end{cases}$$

For the spatially variant envelope equation (A.2) we found that $n_{max}=4$ is in most circumstances sufficient.

References

[1] W. Baumeister, Electron tomography: towards visualizing the molecular organization of the cytoplasm, Current Opinion in Structural Biology 12 (2002) 679–684.

[2] J. Zhu, P.A. Penczek, R. Schröder, J. Frank, Three-dimensional reconstruction with contrast transfer function correction from energy-filtered cryoelectron micrographs: procedure and application to the 70S *Escherichia coli* ribosome, Journal of Structural Biology 118 (1997) 197–219.

[3] G.E. Murphy, J.R. Leadbetter, G.J. Jensen, In situ structure of the complete *Treponema primitia* flagellar motor, Nature 442 (2006) 1062–1064.

[4] J. Liu, A. Bartesaghi, M.J. Borgnia, G. Sapiro, S. Subramaniam, Molecular architecture of native HIV-1 gp120 trimers, Nature 455 (2008) 109–113.

[5] M. van Heel, B. Gowen, R. Matadeen, E.V. Orlova, R. Finn, T. Pape, D. Cohen, H. Stark, R. Schmidt, M. Schatz, A. Patwardhan, Single-particle electron cryo-microscopy: towards atomic resolution, Quarterly Reviews of Biophysics 33 (2000) 307–369.

[6] A. Philippsen, H.-A. Engel, A. Engel, The contrast-imaging function for tilted specimens, Ultramicroscopy 107 (2007) 202–212.

[7] J.J. Fernández, S. Li, R.A. Crowther, CTF determination and correction in electron cryotomography, Ultramicroscopy 106 (2006) 587–596.

[8] H. Winkler, K.A. Taylor, Focus gradient correction applied to tilt series image data used in electron tomography, Journal of Structural Biology 143 (2003) 24–32.

[9] J.A. Mindell, N. Grigorieff, Accurate determination of local defocus and specimen tilt in electron microscopy, Journal of Structural Biology 142 (2003) 334–347.

[10] Q. Xiong, M.K. Morphew, C.L. Schwartz, A.H. Hoenger, D.N. Mastronarde, CTF determination and correction for low dose tomographic tilt series, Journal of Structural Biology 168 (2009) 378–387.

[11] G. Zanetti, J.D. Riches, S.D. Fuller, J.A.G. Briggs, Contrast transfer function correction applied to cryo-electron tomography and sub-tomogram averaging, Journal of Structural Biology 168 (2009) 305–312.

[12] Y. Wan, W. Chiu, Z.H. Zhou, Full contrast transfer function correction in 3D cryo-EM reconstruction, in: IEEE Proceedings of ICCCAS, vol. 2, 2004, pp. 960–964.

[13] G.J. Jensen, R.D. Kornberg, Defocus-gradient corrected back-projection, Ultramicroscopy 84 (2000) 57–64.

[14] I.G. Kazantsev, J. Klukowska, G.T. Herman, L. Cernetic, Fully three-dimensional defocus-gradient corrected backprojection in cryoelectron microscopy, Ultramicroscopy 110 (2010) 1128–1142.

[15] J.N. Dubowy, G.T. Herman, An approach to the correction of distance-dependent defocus in electron microscopic reconstruction, in: IEEE International Conference on Image Processing, ICIP, vol. 3, 2005, pp. 748–751.

[16] I.G. Kazantsev, G.T. Herman, L. Cernetic, Backprojection-based reconstruction and correction for distance-dependent defocus in cryoelectron microscopy, in: IEEE International Symposium on Biomedical Imaging: From Nano to Macro, ISBI, 2008, pp. 133–136.

[17] L. Reimer, H. Kohl, Transmission Electron Microscopy, fifth ed., Springer-Verlag, Berlin, 1984.

[18] A.C. Kak, M. Slaney, Principles of Computerized Tomographic Imaging, IEEE Service Center, 1988.

[19] M. Frigo, S.G. Johnson, The design and implementation of FFTW 3, Proceedings of the IEEE 93 (2005) 216–231.

[20] A. Dutt, V. Rokhlin, Fast fourier transforms for nonequispaced data, SIAM Journal on Scientific Computing 14 (1993) 1368.

[21] A. Dutt, V. Rokhlin, Fast Fourier transforms for nonequispaced data II, Applied and Computational Harmonic Analysis 2 (1995) 85–100.

[22] L. Greengard, J.-Y. Lee, Accelerating the nonuniform fast Fourier transform, SIAM Review 46 (2004) 443.

[23] S. Matej, J.A. Fessler, I.G. Kazantsev, Iterative tomographic image reconstruction using Fourier-based forward and back-projectors, IEEE Transactions on Medical Imaging 23 (2004) 401–412.

[24] A.G. Ramm, A.I. Katsevich, The Radon Transform and Local Tomography, CRC, 1996.

[25] E.T. Quinto, O. Öktem, Local tomography in electron microscopy, SIAM Journal on Applied Mathematics 68 (2008) 1282–1303.

[26] M. Vulovic, B. Rieger, L.J. van Vliet, A.J. Koster, R.B.G. Ravelli, A toolkit for the characterization of CCD cameras for transmission electron microscopy, Acta Crystallographica Section D 66 (2010) 97–109.

[27] M. van Heel, M. Schatz, Fourier shell correlation threshold criteria, Journal of Structural Biology 151 (2005) 250–262.

[28] M. van Heel, Similarity measures between images, Ultramicroscopy 21 (1987) 95–100.

[29] P. Penczek, J. Zhu, R. Schröder, J. Frank, Three dimensional reconstruction with contrast transfer compensation from defocus series, Scanning Microscopy 11 (1997) 147–154.

[30] D.J. DeRosier, Correction of high-resolution data for curvature of the Ewald sphere, Ultramicroscopy 81 (2000) 83–98.